Hindawi
International Journal of Energy Research
Volume 2024, Article ID 2883918, 12 pages
https://doi.org/10.1155/2024/2883918

Research Article

Corrosion Behavior of Candidate Structural Materials for Molten Salt Reactors in Flowing NaCl-$MgCl_2$

Taeho Kim, Dong Jun Shin, Dalsung Yoon, Eun-Young Choi, and Chang Hwa Lee

Advanced Fuel Cycle Technology Development Division, Korea Atomic Energy Research Institute, 111, Daedeok-daero 989 beon-gil, Yuseong-gu, Daejeon 34057, Republic of Korea

Correspondence should be addressed to Taeho Kim; taehokim90@gmail.com

Received 11 January 2024; Revised 11 April 2024; Accepted 13 April 2024; Published 27 April 2024

Academic Editor: Sanjay Basumatary

Abstracts. A high-temperature molten salt natural convection loop was designed and manufactured for chloride-based salts. NaCl-$MgCl_2$ salt was prepared and injected into the loop. Corrosion coupons composed of SS304, SS316L, and high-Ni alloys were also prepared as candidate structural materials for molten chloride salt reactors. After a corrosion experiment was conducted for 500 h, the salt was drained from the loop to the drain tank; inductively coupled plasma optical emission spectroscopy was used to investigate metal dissolution from the materials into the salt. The corroded materials were analyzed using scanning electron microscopy and energy-dispersive X-ray spectroscopy to calculate the corrosion rate. Materials exposed to NaCl-$MgCl_2$ molten salt showed varying levels of corrosion resistance. The high-Ni alloy demonstrated the highest resistance, followed by SS316L and SS304. Furthermore, corrosion products were observed to migrate along the molten salt through natural convection, eventually depositing onto the surface of the high-Ni alloy in the cold leg of the loop.

1. Introduction

Molten salt is a liquid, that is, a melted chemical compound of alkali and acid at high temperatures; in general, it is transparent and resembles water. Many types of molten salts exist because of the various combinations of alkalis and acids. Molten salts, which are ionic compounds in liquid form at high temperatures, are composed of positively charged ions (cations) and negatively charged ions (anions) held together by strong electrostatic forces. They result from combinations of alkalis like lithium, sodium, potassium, rubidium, and cesium, along with acids such as fluorine, chlorine, bromine, and iodine. These combinations create various types of molten salts including alkali halides (NaCl, KBr, and LiI) and mixed salts (LiF-KF, NaCl-$MgCl_2$) and complex salts (carbonate, sulfate salt) each with distinct properties and uses.

Molten salt reactors were developed at the Oak Ridge National Laboratory, and molten salt fuel was selected because of its chemical stability. Molten salt reactors can be operated at extremely low pressures owing to the low vapor pressure and high boiling point of the molten salts. In addition, molten salts, especially those based on fluoride and chloride, can dissolve most nuclear materials such as uranium, thorium, and other minor actinide elements. Because most types of molten salts have high melting points (exceeding 400°C), if the vessels or pipes for molten salt reactors break, the leaked molten salt will freeze and prevent the release of radioactive materials [1]. Nuclear materials like fluoride-based molten salts, such as LiF-BeF_2-ThF_4-UF_4, can effectively dissolve uranium tetrafluoride (UF_4) and thorium tetrafluoride (ThF_4), along with other actinides and fission products generated during reactor operation. Similarly, chloride-based molten salt reactors have the capacity to dissolve uranium tetrachloride (UCl_4), thorium tetrachloride ($ThCl_4$), and other relevant nuclear materials. This solubility of nuclear materials within molten salts enables continuous fuel reprocessing and removal of fission products and facilitates online refueling and maintenance operations, thus contributing to enhanced safety, efficiency, and reduced nuclear waste generation in molten salt reactor technology.

Current research on the corrosion behavior of molten chloride salts is aimed at understanding why they degrade, especially in high-temperature environments like molten salt reactors and concentrated solar power systems. Factors such as temperature, composition, impurities, and protective coatings to see how they affect corrosion have been considered from previous literatures [2–8]. Progress has been made, but challenges remain in ensuring long-term stability and reliability. Compared to fluoride salts, research on chloride salts, which are also used in molten salt reactors, is not as extensive. More studies are needed to understand how chloride salts corrode and to improve the performance of systems using them.

The molten chloride salt reactor is an advanced nuclear reactor that employs a molten uranium chloride salt system to generate heat for electricity production. In contrast to conventional solid fuel reactors, the molten chloride salt reactor is designed as a fluid fuel reactor wherein the fissile material is dissolved in the heat transfer fluid. The precursor of the molten chloride salt reactor is the Molten Chloride Reactor Experiment; this research reactor has been used to investigate the fundamental physics of chloride salt-fueled reactors. Molten salt fuel reactors offer numerous advantages over conventional solid fuel reactors. These include an increased fuel economy, low-pressure operation, and strong temperature-driven negative reactivity feedback. Additionally, the high-temperature operation of molten salt reactors facilitates the use of a closed fuel cycle, thus minimizing the generation of nuclear waste. The benefits of molten salt fluid fuel reactors have been comprehensively analyzed in previous studies [7, 9].

Material compatibility tests have been conducted since the Aircraft Nuclear Propulsion program at the Oak Ridge National Laboratory in the 1950s, in addition to the Molten Salt Reactor Experiment and the Molten Salt Breeder Reactor programs in the 1960s and 1970s, respectively [10–17]. One of the challenges associated with these programs is the mass transfer resulting from the interaction between the structural materials and molten salt; consequently, these materials may be deposited in the cold sections of the system, thereby blocking the salt flow. This phenomenon has been extensively studied and documented for fluoride molten salts, especially in the Molten Salt Reactor Experiment program and in recent research from the Oak Ridge National Laboratory [17].

Thermal convection loops have emerged as the primary testing method for evaluating molten salt corrosion, particularly molten fluoride corrosion [18]. Conducting corrosion studies with a designed loop is necessary for understanding how candidate structural materials perform in molten salt reactors using chloride salts. This setup allows to simulate real conditions and observe how materials react to exposure to molten salts at high temperatures. By studying corrosion in this controlled environment, it is able to identify which materials are more resistant to degradation and which ones may need improvement. These results helps in selecting the most suitable materials for building molten salt reactors, ensuring their safety and reliability. Thermal convection loops are typically designed to test for corrosion by creating a buoyant force through temperature-induced density gradients. A pressure differential based on density change is generated by placing a hot leg below a cold leg. These thermal convection loops can induce mass transport, which cannot be achieved in isothermal corrosion tests such as autoclave experiments [19]. In isothermal autoclave tests, corrosion only occurs to a depth that satisfies the solubility requirements of the liquid at operating temperatures. However, in thermal convection tests, the material is cyclically transported from the hot to cold leg positions based on redox reactions, for which the equilibrium constants vary as a function of temperature.

Thermal gradient-pumped loops have flow velocities that are several orders of magnitude higher than those of thermal convection loops and can more accurately simulate reactor operating conditions [15]. Although no study on corrosion in molten salt thermal convection has been as comprehensive as that conducted by the Oak Ridge National Laboratory, the corrosion of molten chloride salts in thermal convection loops has been evaluated by other legacy programs [20, 21].

In a typical molten salt thermal convection loop, corrosion is most pronounced in the hot leg, which exhibits high reaction kinetics; consequently, the most corrosive alloying element in the alloys is converted into a salt. The nobility of an alloying element in an alloy can be determined by comparing the relative Gibbs free energies of formation per mole of anion. In fluoride and chloride systems, common alloying elements that are ranked according to decreasing nobility are molybdenum, nickel, iron, and chromium [22, 23]. Chromium forms the most stable corrosion product salt and is attacked more aggressively than other elements within a given alloy. However, despite the identical ranking order, chloride systems have a smaller Gibbs free energy difference between the salt and alloy formation energies. This is expected to establish a chemical equilibrium in chloride systems, which inherently have a higher tendency to corrode than fluoride systems.

As the molten salt flows through a thermal convection loop, corrosion product salts are formed and readily dissolve in the bulk fluid [24]. As the salt enters the cold leg, the decreasing temperature alters the equilibrium constants of the corrosion reactions, thereby reversing the corrosion reactions and forming precipitates of solid metal particulates in the system [5, 9]. These precipitates may be deposited on the inner walls of the loop, constrict the flow, diffuse into the alloy, or remain suspended in the salt [22, 24, 25]. After the corrosion products are deposited in the cold leg, the salt returns to the hot leg, where the equilibrium constants shift again toward the corrosion of the alloy, thus restarting the cycle. Particularly, the thermal gradient in the system prevents it from attaining chemical equilibrium, which is a key difference from isothermal autoclave testing. This difference is valuable because it mimics the corrosion occurring in a molten salt reactor, wherein salt flows from a hot reactor core to a heat exchanger. These phenomena in fluoride salts are concisely discussed in the previous study [26, 27].

Natural convection loops were initially developed as a simple and reliable method for evaluating molten salt

corrosion, whereas high-temperature pumps and seals were developed for forced convection loops, which are more representative of the conditions within a reactor. Forced flow loops have since been operated and have demonstrated that the flow velocity minimally affects corrosion rates, further supporting the relevance of thermal convection loops [28]. Despite their relatively simple design, thermal convection loops have been demonstrated as valuable tools for corrosion testing, as evidenced by their successful operation over many years during experiments such as the Molten Salt Reactor Experiment and its predecessor, the Aircraft Reactor Experiment. These experiments have provided important insights into the behavior of molten salt systems and contributed to the ongoing development of advanced nuclear technologies.

Molten chloride salts are important for use as heat transfer fluids; however, research on their corrosion behavior is limited compared to that of fluoride salts. Most studies have involved short-term static tests, isothermal autoclave tests, or accelerated electrochemical corrosion testing, which do not consider the thermal-gradient mass transport that occurs in reality. Moreover, the reported corrosion rates of chloride salts are considerably varied, making it difficult to draw clear conclusions. To address this gap, a natural convection chloride salt loop was designed, and corrosion studies were conducted with the loop. The findings from this study can elucidate the corrosion behavior of candidate structural materials for molten salt reactors in chloride salts and provide guidance for selecting alloys applicable to chloride-based molten salt reactors.

2. Experimental

2.1. Salt and Sample Preparation. A molten salt mixture consisting of NaCl-$MgCl_2$ (57–43 mol%) was prepared from commercially available NaCl (99.5%, 1 kg, Junsei) and $MgCl_2$ (anhydrous 99%, 1 kg, Alfa Aesar). A total of 8.5 kg salt (3.8 kg NaCl and 4.7 kg $MgCl_2$) was injected into the salt preparation tank. To remove the remaining moisture in the salt, the salt mixture in the salt preparation tank was dried at 117, 185, 242, 304, 350, and 554°C [20, 21]. The following seven reactions occurred at different temperatures:

$$\begin{aligned}
&117^{\circ}\mathrm{C}: MgCl_2 * 6H_2O \rightarrow MgCl_2 * 4H_2O + 2H_2O\\
&185^{\circ}\mathrm{C}: MgCl_2 * 4H_2O \rightarrow MgCl_2 * 2H_2O + 2H_2O\\
&242^{\circ}\mathrm{C}: MgCl_2 * 2H_2O \rightarrow MgCl_2 * H_2O + H_2O\\
&304^{\circ}\mathrm{C}: MgCl_2 * H_2O \rightarrow MgCl_2 + H_2O\\
&182^{\circ}\mathrm{C}: MgCl_2 * 2H_2O \rightarrow MgOHCl + HCl + H_2O\ (\text{partial hydrolysis})\\
&350^{\circ}\mathrm{C}: MgCl_2 * H_2O \rightarrow MgOHCl + HCl\ (\text{complete hydrolysis})\\
&554^{\circ}\mathrm{C}: MgOHCl \rightarrow MgO + HCl
\end{aligned} \tag{1}$$

Although $MgCl_2$ is anhydrous, it can exist as a hydrate owing to various possibilities. Complex reactions such as those described above can be used to dehydrate $MgCl_2$. However, at 182 and 350°C, $MgCl_2$ reacts with H_2O to produce HCl, and at 554°C, MgOHCl decomposes to produce HCl. Therefore, a large amount of HCl is released during the preparation of the NaCl-$MgCl_2$ salt. If HCl is not removed, it can corrode the equipment used in the experiments and the natural circulation loops of molten salts. Therefore, a neutralization device is necessary for HCl removal. Accordingly, an acid-resistant vacuum pump was installed in the salt pretreatment device to create vacuum, and HCl was discharged into the atmosphere using a scrubber.

During the entire drying process, a vacuum of 0.1 MPa was maintained to remove HCl and moisture from the salt. Figure 1 illustrates the system used for removing moisture from the salt. The Ar-filled glovebox for the salt pretreatment system was controlled with O_2 and H_2O under 1 ppm to prevent moisture from coming into contact with the salts at any stage. The salt was analyzed using inductively coupled plasma optical emission spectrometry (ICP-OES) at Chungbuk National University, and the results are shown in Table 1. Owing to the absence of a reliable technique for quantifying the moisture content, only the presence of metallic impurities has been reported.

Three alloys were used in this study: SS304, SS316L, and a high-Ni alloy. The alloy compositions are listed in Table 2. The composition was measured using a spark optical emission spectrometer (Spark-OES) at the Korea Institute of Materials Science. For each alloy, 12 samples (10 mm × 15 mm × 1 mm) were prepared for the corrosion experiment in a natural convection loop and arranged in pure Ni wire. Two Ni wires were prepared using 18 samples of SS304, SS316L, and a high-Ni alloy for the hot and cold legs of the natural convection loop, as shown in Figure 2. These two wires were suspended in the vertical portions of the loop: one in the hot leg and the other in the cold leg.

2.2. Molten Salt Loop Construction. To simulate the molten salt reactor environment, a high-temperature natural convection loop was designed and constructed. A pretreatment tank, salt reservoir, and drain tank were installed for the natural convection loop with a 25.4 mm (1 inch) SS316L tube. Figure 3 shows a schematic of the natural convection loop and locations where the temperature of the salt was measured during the experiment (T1–T6). Six thermocouples were placed in the loop: three in the hot leg and the remaining three in the cold leg.

Figure 4 shows the complete system with a heater-covered tube and tanks. Table 3 lists the name and power of each heater installed in the natural convection loop. Each tank has its own heater, and the total power of the loop is 6.03 kW. The target fuel salt for the molten salt reactor is a high-assay low-enriched uranium-based NaCl-$MgCl_2$ salt; however, only NaCl-$MgCl_2$ salt was used in this study.

2.3. Loop Operation for Corrosion Test. The prepared chloride salt remained in the pretreatment tank and was connected directly to the natural convection loop. Subsequently, the two sample chains with corrosion coupons, comprising candidate structural materials (SS304, SS316L, and high-Ni alloy) for the molten chloride salt reactor, were introduced into each leg of the loop. To fill the

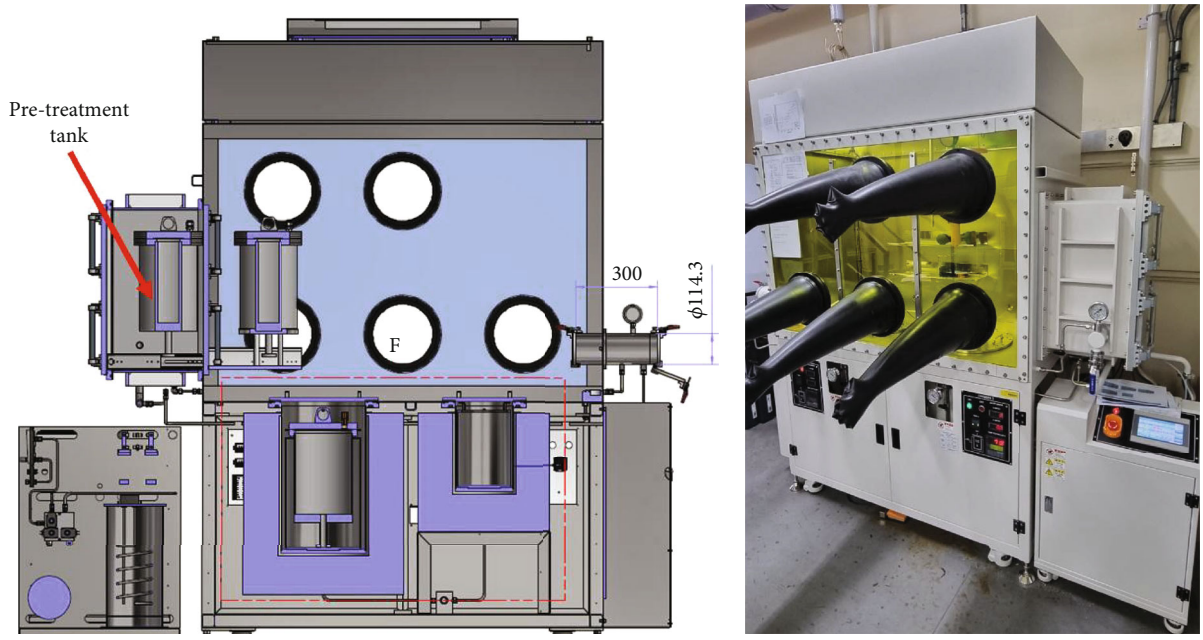

(a) (b)

Figure 1: The pretreatment system for molten salt to remove moisture in the salt. (a) A schematic for the pretreatment system. The pretreatment tank for a natural convection loop can be installed in the system. (b) An image of the pretreatment system in Korea Atomic Energy Research Institute (KAERI).

Table 1: The results of ICP analysis of the salt before and after the corrosion experiment. Precorrosion sample is the salt from just after pretreatment process with removing moisture (unit: ppm, detection limit < 12.5 ppm).

Sample	Element					
	Na	Mg	Fe	Cr	Ni	Mn
Precorrosion	152000	119600	300.5	33.8	N.D	N.D
Postcorrosion			460.7	218	N.D	18.3

entire natural convection loop with salt, all the heaters installed in the loop were switched on. The heater and salt temperatures for the melting process, stabilization, and normal operation are presented in Figures 5 and 6, respectively. The mixture was melted for 8 h (Figure 6). The measured temperatures of T1–T6 increased step-by-step, and when T6 reached the melting point of the NaCl-$MgCl_2$ eutectic (460°C), the temperatures of T1–T6 became equal, and the eutectic molten salt began to be circulated. This point was defined as the fully melted salt point. The subsequent stage was the stabilization phase, which continued for approximately 4 h. All heaters, except the hot leg heater, were switched off during this phase; the natural circulation loop was operated using only the output of the hot leg. The temperature of the hot leg was set at 950°C (Figure 5). After 5 h, the natural circulation loop was operated under normal conditions. In summary, the salt mixture after pretreatment are in the pretreatment tank as solid state, and to transfer the molten salt from the pretreatment tank to the salt reservoir and loop, the temperatures of the loop and salt reservoir are raised using heaters to the melting point of the molten salt. Subsequently, the temperature of the pretreatment tank is also elevated to above the melting point, ensuring that the molten salt in the pretreatment tank fills up from the bottom of the loop due to gravity. This process is designated as the stabilization phase. Following this phase, operation solely relies on the heaters in the hot leg, which is considered the normal condition.

Figure 6(b) shows an enlarged image of the temperature data from the stabilization to the normal operation phase. The actual starting point of the experiment is indicated by a red arrow, and the operation proceeded for 500 h from the starting point. The highest temperature of T6 in the hot leg was approximately 580°C, and the lowest temperature of T1 in the cold leg was approximately 500°C during the entire period of operation. Each heater in the molten salt natural convection loop was equipped with its own current sensor to calculate the molten salt flow rate based on the heating power supplied to the hot and cold legs of the molten salt natural convection loop. During the experiment, a vacuum pump connected to a fill pot was operated to maintain a vacuum below 5 mTorr. After 500 h of corrosion, the salt was drained from the loop into the drain tank for ICP-OES, and metal dissolution from the structural materials into the salt was investigated.

Two sample chains were removed from the cold and hot legs and cleaned with acetone, ethanol, and deionized water. Thirty-six samples were separated from the sample chains, and their weight changes before and after the corrosion experiment were measured using a high-precision electronic balance (MS105DU, Mettler Toledo). Eighteen of these samples were mounted and polished for scanning electron

Table 2: Chemical compositions of corrosion samples for this study (unit: wt.%).

Sample	Element											
	Ni	Mo	Cr	Fe	Si	Mn	W	Cu	Co	C	Al	Ti
High-Ni alloy	70.57	15.83	8.05	4.96	0.20	0.53	0.28	0.011	0.041	0.01	0.25	0.20
SS316L	10.00	1.66	18.00	Bal.	0.75	2.00	—	—	—	0.08	—	—
SS304	10.00	—	18.18	Bal.	0.57	1.75	—	—	—	0.051	—	—

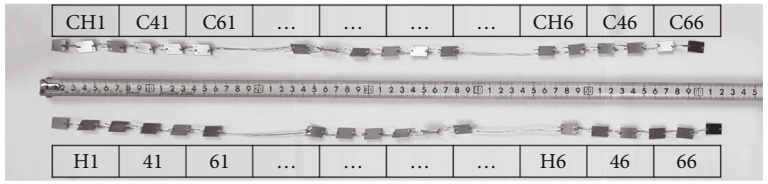

Figure 2: Two Ni wires with 36 samples of SS304, SS316L, and a high-Ni alloy. Samples with capital letter "C" are for the cold leg and without are for the hot leg of natural convection loop.

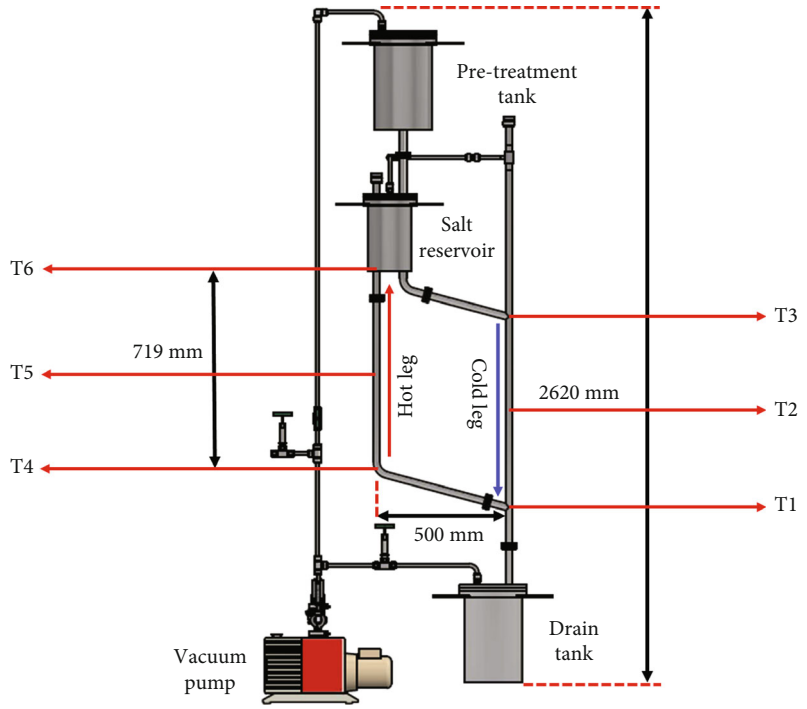

Figure 3: A schematic of a high-temperature molten salt natural convection loop in KAERI.

microscopy (SEM) and energy-dispersive X-ray spectroscopy (EDS) analyses using a Crossbeam 540 instrument (ZEISS).

3. Results and Discussion

3.1. Salt Composition and Weight Gain/Loss Analysis. Table 1 presents the results of the ICP-OES analysis of the salt before and after the corrosion experiment. The concentrations of Fe and Cr were 301 and 34 ppm, respectively, before the experiment, but they increased to 461 and 218 ppm, respectively, after the experiment. In addition, trace amounts of Mn were present before the experiment, which increased to 18 ppm thereafter. Fe, Cr, and Mn are all elements of SS316L, SS304, and the high-Ni alloy (Table 2), indicating that they were leached into the salt during the corrosion experiment.

Figure 7 shows the weight changes of the samples before and after the corrosion experiments. The red and blue dots represent weight changes in samples from the hot and cold legs, respectively. The squares, circles, and triangles indicate the weight changes in the high-Ni alloy, SS304, and SS316L samples, respectively. The weight loss of SS304 was the highest under both the cold and hot leg conditions, indicating that the corrosion behavior of SS304 in the molten salt was the least satisfactory. The corrosion progressed in the following order: SS304, SS316L, and high-Ni alloys. Notably, when the cold and hot leg temperatures were similar (T2–T4 positions, T3–T5 positions), the weight loss in the hot leg was slightly higher

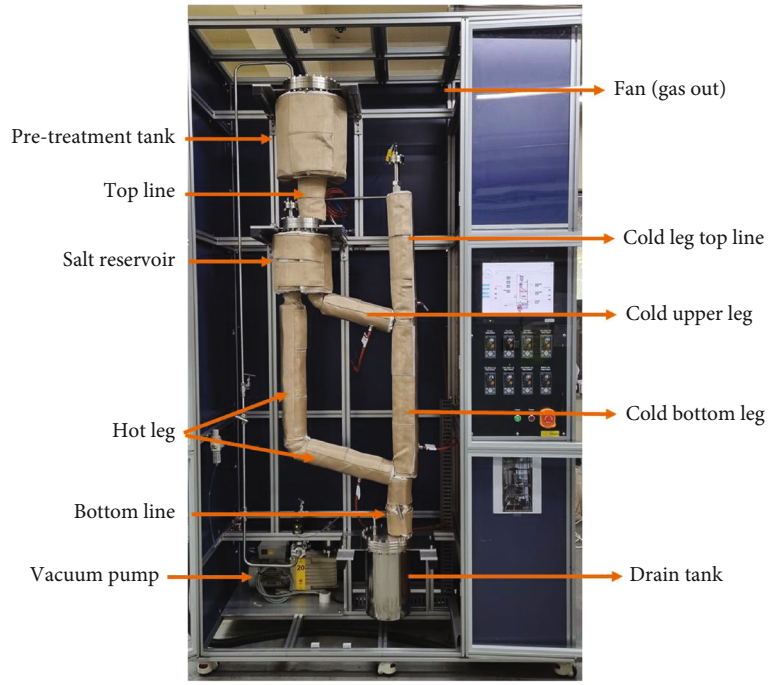

Figure 4: An image of natural convection loop in KAERI.

Table 3: The names and powers of each heater installed in the natural convection loop.

Heater name	Power (kW)
Pretreatment tank	1.8
Top line	0.3
Salt reservoir	1.1
Hot leg	1.4
Cold leg top line	0.3
Cold upper leg	0.37
Cold bottom leg	0.46
Bottom line	0.3
Sum	6.03

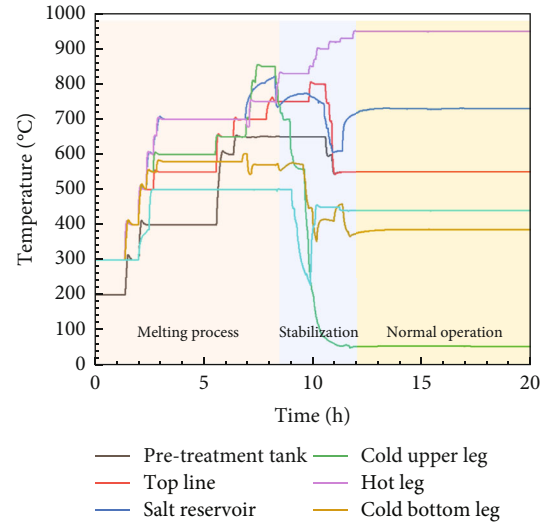

Figure 5: The heater temperature during melting, stabilization, and normal operation of the natural convection loop.

than that in the cold leg, indicating mass transport in the natural circulation loop. Moreover, only the high-Ni alloy samples installed in the cold leg demonstrated weight gain, indicating that deposits may have accumulated on the high-Ni alloy surface installed in the cold leg.

3.2. Microstructural Analysis. Eighteen samples, consisting of three samples each of SS304, SS316L, and high-Ni alloy from both the cold and hot legs, were analyzed for their microstructure. Each sample was cleaned in DI water at 30°C for more than 30 min to remove any residual salt and then mounted and polished. SEM and EDS analyses were subsequently performed.

Figure 8 shows the SEM analysis results for the hot leg samples. The data in Figure 8(a) represents the analysis results of the high-Ni alloy, SS304, and SS316L at the T6 position from left to right; Figures 8(b) and 8(c) represent the data at the T5 and T4 positions, respectively. The SEM analysis results also showed damage attributed to the corrosion of the SS304 material, similar to the results in Figure 7, and this was also evident in the roughness of the surface. Particularly, in the highest temperature data of Figure 8(a), SS304 exhibited corrosion exceeding 40 μm. However, in the lowest temperature data of Figure 8(c), corrosion was scarcely observed in the Ni alloy and SS316L in the hot leg.

Figure 9 shows the SEM analysis results of the cold leg samples. The data in Figure 9(a) from the left represent the analysis results of the high-Ni alloy, SS304, and SS316L at the T3 position, and Figures 9(b) and 9(c) represent the data

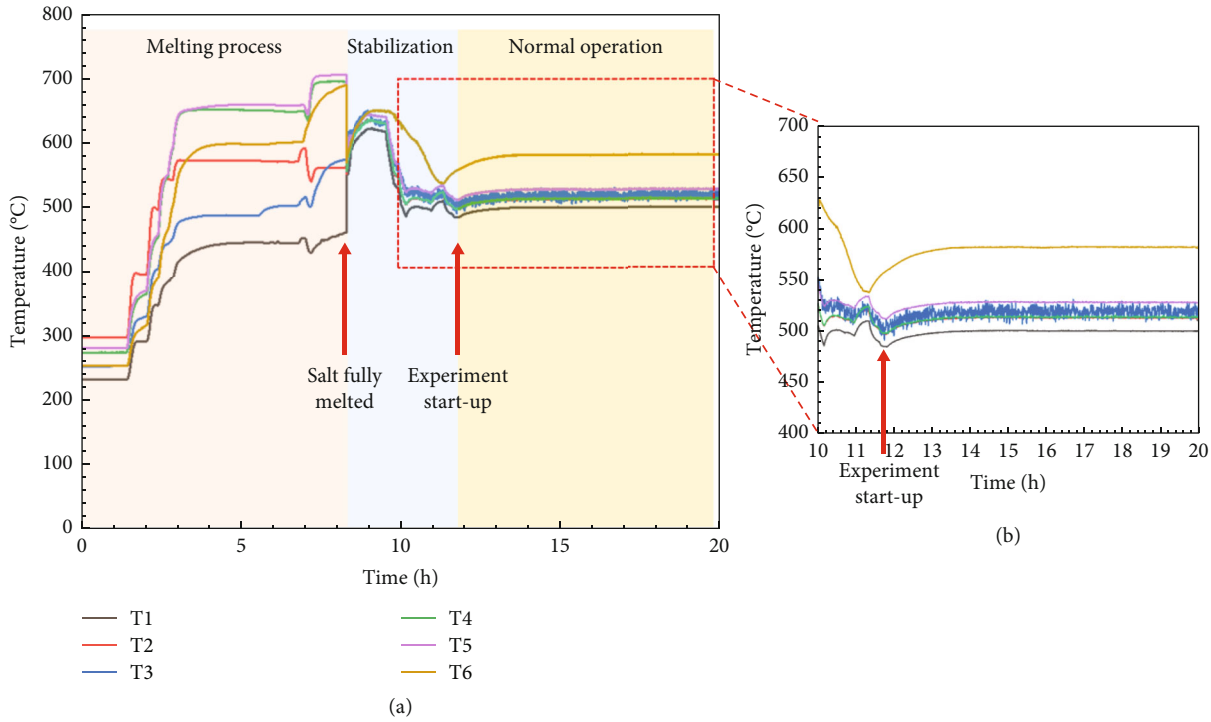

Figure 6: The salt temperature during melting, stabilization, and normal operation of the natural convection loop. (a) The salt temperature up to first 20 h from the heater on. (b) An enlarged view between stabilization and normal operation. The experimental start time was defined as the moment when the temperature of T6 begins to rise from its lowest point.

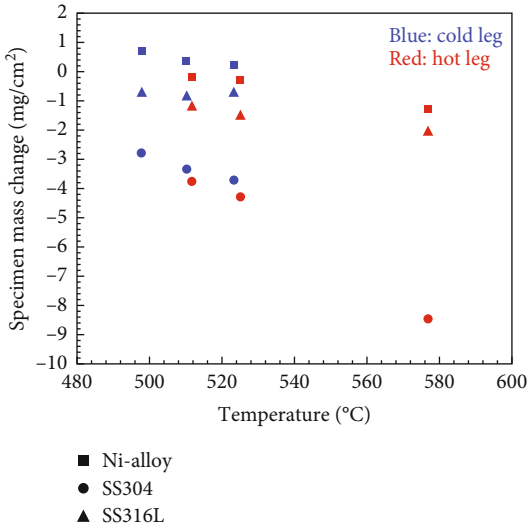

Figure 7: The weight change graph of the samples before and after the corrosion experiment in natural convection loop.

at the T2 and T1 positions, respectively. Similar to the results shown in Figure 7, the damage due to the corrosion of the SS304 matrix was most prominent in the SEM analysis results of the cold leg samples. However, in contrast to the results for the hot leg samples, in the highest temperature data of the cold leg, SS304 exhibited corrosion of approximately 10 μm. In addition, a unique phenomenon was observed in the microstructure of the high-Ni alloy, wherein weight gain was detected. A deposit was observed between the wavy surfaces, only in CH3 and CH5 of the high-Ni alloy. EDS analysis was performed to analyze the composition of this deposit (Figure 10).

Figure 10(a) shows the EDS mapping results of the CH3 sample. The flat surface corresponds to the high-Ni alloy matrix, on which deposits of Ni, Fe, Mg, and O were detected. Ni and Fe are presumed to have originated from the structural material and pipes and then adhered to the surface. Mg and O are considered to be traces of MgO present in the NaCl-$MgCl_2$ eutectic salt that was used in the pretreatment, and these traces subsequently adhered to the matrix surface. Figure 10(b) shows the EDS line scan results for the CH3 sample. EDS analysis revealed a deposit on the sample surface with high Fe and low Cr contents.

3.3. Corrosion in Flowing Molten Salt. To calculate the flow rate of the molten salt in the natural circulation loop, the amount of heat supplied to the hot leg and that lost from the cold leg must be determined. In this study, a natural circulation loop of molten salt was designed, and experiments were conducted with power meters installed on each heater to measure the amount of current applied to the heaters. Figure 6 shows that the molten salt was maintained at a constant temperature in both the hot and cold legs during normal operation. The power supplied to the hot leg heater during normal operation was 1.386 kW, which was obtained by multiplying the voltage applied to the 220 V heater with the current measured from the 6.3 A heater. During normal operation, because the heat supplied to the hot leg and that lost from the cold leg attained equilibrium, a total energy of 1.386 kW was supplied

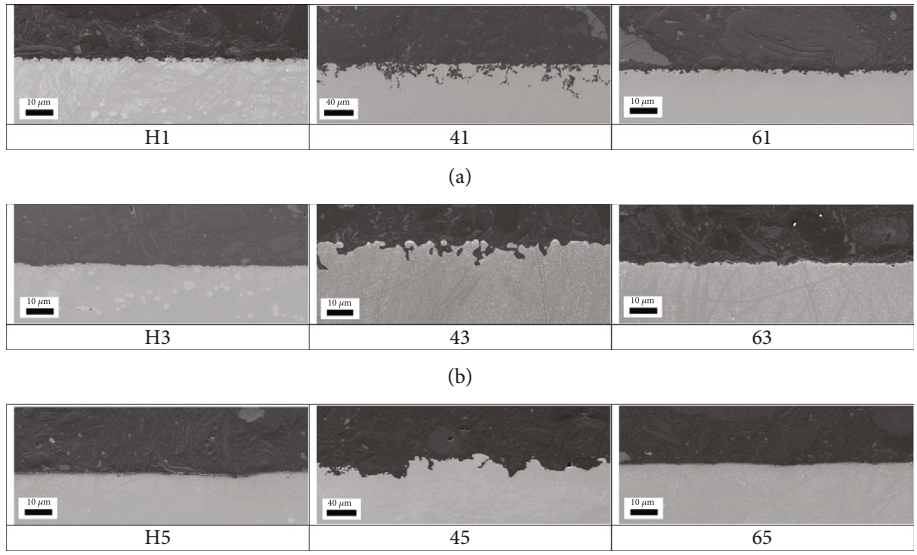

Figure 8: The SEM analysis results of hot leg samples. (a) SEM images of corroded samples at the T6 position, (b) at the T5 position, (c) at the T4 position.

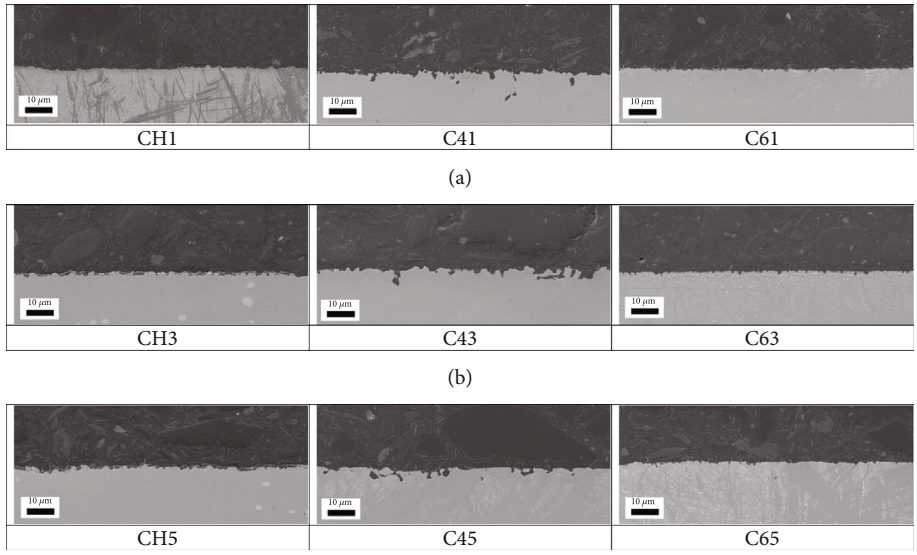

Figure 9: The SEM analysis results of cold leg samples. (a) SEM images of corroded samples at the T3 position, (b) at the T2 position, (c) at the T1 position.

to the hot leg and lost from the cold leg. This could be attributed to the loss of heat from the top to the bottom of the cold leg owing to the flow of molten salt, and the temperature difference between the two points was 73.2°C.

In Equation (2), Q is calculated to be 1.386 kW, and C_p is the specific heat capacity of the NaCl-$MgCl_2$ eutectic salt, which is 0.858 J/g K. The density of the eutectic salt is 2.23 g/cm^3; therefore, using Equation (2), the flow rate of the molten salt in a natural circulation loop with a 1-inch outer diameter can be calculated as 2.48 cm/s (Table 4).

$$Q = C_p \dot{m} \Delta T. \quad (2)$$

According to the data presented in Figures 8 and 9, only the samples fabricated from high-Ni alloys had a visible layer deposited on their surfaces in the cold leg of the loop. This was observed in the CH3 and CH5 samples, which were exposed to lower temperatures. In addition, Figure 7 shows that only the high-Ni alloys in the cold leg and two samples in the colder part of the hot leg gained mass, suggesting that a mixed mode of corrosion occurred in the corroded samples, accompanied by the formation of a deposit. As demonstrated by the EDS analysis results (Figure 10), the deposit appears to be rich in MgO, Fe, and Ni. MgO is presumed to be the product of the purification of $MgCl_2$. A similar phenomenon has been observed in previous studies, suggesting that MgO is formed

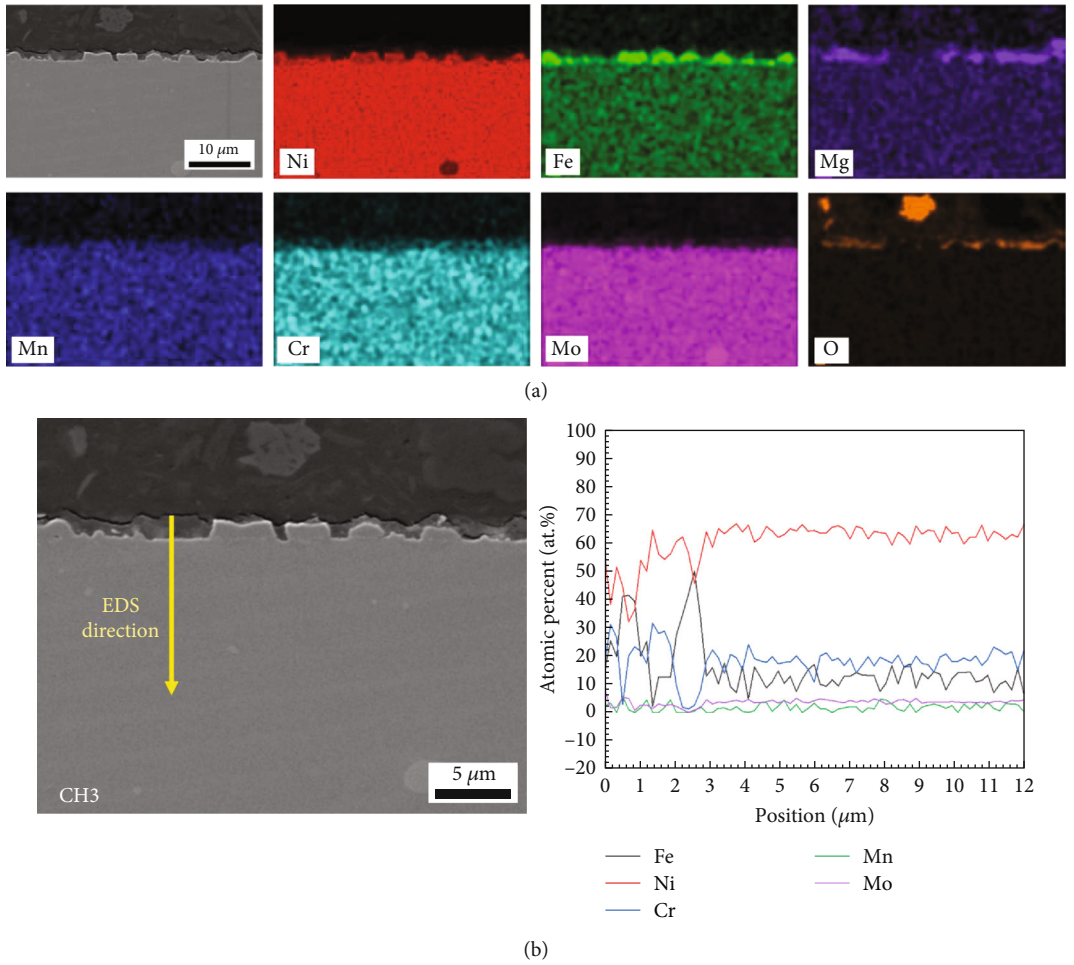

Figure 10: (a) The EDS mapping analysis of the CH3 sample. (b) The EDS line scan results for the CH3 sample.

Table 4: The properties of NaCl-$MgCl_2$ eutectic salt in this study.

Total weight	8.5 kg
Heat capacity	0.858 J/K
Density	2.23 g/cm^3
Melting point	460°C

during the purification process and subsequently adsorbed onto the metal surface [29]. In contrast, Ni and Fe are considered to have been leached from the loop piping and sample, subsequently floating within the molten salt, and being deposited onto the low-temperature region of the sample. This observation further indicates the occurrence of mass transport within the loop.

Furthermore, to calculate the corrosion rate of each candidate structural material in the natural circulation loop environment, Equation (3) was employed to determine the corrosion rate for each material.

$$\text{Corrosion rate } (\mu\text{m/year}) = (365)\bullet 10000\left(\frac{\Delta m}{\rho}\bullet S\bullet T\right), \quad (3)$$

where Δm is the weight change (g), ρ is the density of the sample (g/cm^3), S is the surface area of the sample (cm^2), and T is the total corrosion time (d) [30].

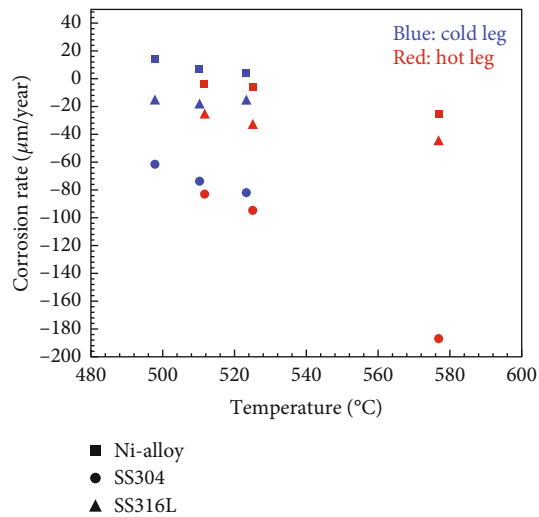

Figure 11: Annual corrosion rate data for each candidate material tested in the natural convection loop.

Figure 11 presents the annual corrosion rate data for each candidate material tested in the natural circulation loop. The blue and red data points correspond to the

corrosion rates of the cold and hot leg specimens, respectively. The square, circular, and triangular markers indicate the corrosion rate data for the high-Ni alloys SS304 and SS316L, respectively. Positive corrosion rates were observed only in the high-Ni alloy specimens in the cold leg, and the corrosion performance of SS316L was the most unfavorable. Under the same temperature conditions, the corrosion rate in the hot leg experiments was higher than that in the cold leg experiments, providing further evidence for mass transport in the natural convection loop.

3.4. Discussion. In this study, corrosion experiments on chloride salts, which have limited data available thus far, were conducted using a natural convection loop. Consistent with findings reported by Raiman et al. [17], corrosion was observed in stainless steel and high-Ni alloy when exposed to chloride salts, similar to fluoride salts. This resulted in the formation of a chromium depletion region within the metal matrix and an increase in the concentrations of Cr and Fe within the salt. However, due to a lack of diverse corrosion experimental results specifically on chloride salts and certain assumptions made in the calculation of salt flow within the natural convection loop (such as neglecting heat loss from the heater and assuming all heat loss occurs in the cold leg), future research is aimed at obtaining corrosion results applicable to practical molten salt reactors by comparing them with corrosion experiments in microsize loops (approximately 30 cm in height) and static cells using chloride salts.

The findings of this study can be summarized into two main points. Firstly, the corrosion resistance was found to be superior in the order high-Ni alloy, SS316L, and SS304, when exposed to NaCl-$MgCl_2$ molten salt. Secondly, the corrosion product was observed to migrate along the molten salt within the natural convection loop and deposit onto the high-Ni alloy surface in the cold leg.

Corrosion caused by molten salt fuel is primarily driven by several factors. One critical factor is that the typical corrosion resistance mechanism in metals, where protective oxide or other layers form, does not apply to molten salts because they can effectively dissolve these protective layers. So, corrosion in this context is fundamentally determined by thermodynamics. If the system's thermodynamics allow a component of the alloy to dissolve in the molten salt, it will happen. The corrosion rate is then influenced by how quickly the vulnerable metal can move to the exposed surface of the alloy. The presence of cracks and pits significantly accelerates this process, leading to rapid corrosion, especially at the boundaries between alloy grains.

Three different alloys, SS304, SS316L, and high-Ni alloy, were immersed in the eutectic NaCl-$MgCl_2$ salts after purification. The annual corrosion rate of SS304 was 9 times larger than that of high-Ni alloy and 5 times larger than that of SS316L, at hot leg temperature, 580°C. In spite of rigorous efforts to minimize the presence of water and oxygen impurities during the experimental procedure, the inherent hygroscopic nature of $MgCl_2$ introduces a significant challenge in achieving complete desiccation of residual moisture within the NaCl-$MgCl_2$ salt matrix. Even marginal quantities of water and oxygen within the corrosion milieu are prone to engage in intricate chemical interactions with the salt matrix, leading to the generation of HCl and Cl_2 gas. This resultant chemical activity imparts an accelerated impetus to the corrosion kinetics.

The Ni, Cr, and Fe found in the SS304 alloy have a tendency to undergo chemical reactions with HCl and Cl_2 gas. These reactions lead to the creation of specific metal chloride compounds, as shown in reactions (2)–(5). These reactions play a key role in causing high-temperature chlorination-induced corrosion [1, 17, 31–33].

$$\mathrm{Cr} + 2\mathrm{HCl}\,(\mathrm{g}) = \mathrm{CrCl_2} + \mathrm{H_2}\,(\mathrm{g}) \tag{4}$$

$$\mathrm{Fe} + \mathrm{Cl_2}\,(\mathrm{g}) = \mathrm{FeCl_2} \tag{5}$$

$$\mathrm{Ni} + \mathrm{Cl_2}\,(\mathrm{g}) = \mathrm{NiCl_2} \tag{6}$$

$$\mathrm{Cr} + \mathrm{Cl_2}\,(\mathrm{g}) = \mathrm{CrCl_2} \tag{7}$$

Based on Gibbs free energy calculations of the reaction formula, the order of reaction rates for the primary elements in the SS304 alloy when exposed to NaCl-$MgCl_2$ salt follows Cr > Fe > Ni. This implies that Cr experiences a higher rate of attack compared to Fe and Ni, making it the element most susceptible to corrosion [1, 18]. When comparing the compositions of three alloys, it can be observed that SS316L and SS304 have higher Cr concentrations compared to high-Ni alloy. Furthermore, as both SS316L and SS304 are Fe-based alloys, their corrosion resistance in molten salt environments is considered lower than that of high-Ni alloy.

The corrosion products were only detected on the surface of two high-Ni alloys at the cold section, while not at the hot one as shown in Figure 10. The presence of deposits on the interior surfaces of piping or corrosion specimens in the cold leg of a molten salt natural circulation loop has been observed in fluoride-based molten salt experiments such as the Molten Salt Reactor Experiment and in several preceding studies [18, 33]. However, such observations have not yet been confirmed in chloride-based molten salts, and it is important to fully understand the deposit formation mechanism because migration and deposition of the metal would be a significant problem and would be expected to lead to deposition on the coolest surfaces which would be in the heat exchanger.

The reason for deposition occurring only in the cold leg in corrosion experiments can be explained by various factors. This phenomenon is attributed to the characteristics of the molten salt and the thermal conditions of the system. The cold leg section is characterized by relatively lower temperatures within the system. As a result, the cooling rate of the molten salt increases, potentially leading to a reduction in the chemical reaction rates within the molten salt. These conditions can facilitate the formation of deposits. Also, the rapid cooling in the cold leg can induce alterations in the thermodynamic properties of the molten salt. This can affect the chemical equilibria within the molten salt and have an impact on deposit formation. Figures 9 and 10 show that the deposited layer on the high-Ni alloy at the cold leg were

rich in Ni, Fe, Mg, and O. Only three high-Ni alloy samples at the cold leg gained mass as shown in Figure 7. This finding is quite unexpected, as most prior research in this field has primarily focused on studying the transport of chromium (Cr) in molten salts. Furthermore, our work, as shown in Figures 7 and 10, indicates that Cr is the alloy component most significantly depleted by exposure to the salt. This can be also confirmed by the results of ICP analysis of the salt after the corrosion experiment, as shown in Table 1, and this also implies that metal cations diffused from the metal to the salt.

The natural convection loop observation at a single temperature gradient provides insufficient data to elucidate the observed Fe, Ni-rich, and Mg-rich deposits and necessitates further investigation. Notably, similar deposits were observed in alloy 600 thermal convection loop experiments with Cl salts in previous study [34]. Figure 11 shows the annual corrosion rate for each candidate material, and only samples in the cold leg showed weight gain, which is likely due to mass transport-induced deposition on the sample surface rather than loss due to corrosion. Additionally, no Cr deposits were found, but only Ni and Fe deposits and materials appear to be MgO from EDS analysis results. This is similar to the results of the Molten Salt Reactor Experiment research and other flowing loop experiments [12, 14, 18]. Despite these uncertainties from sample analysis, the present results indicate that Ni alloy exhibits reasonable compatibility with NaCl-$MgCl_2$ molten salt at 500 to 580°C, making it a suitable candidate for further molten salt reactor-related assessments. In future studies, we plan to evaluate the corrosion characteristics of other candidate structural materials and the corrosion characteristics of candidate structural materials in a natural convection loop with UCl_3 fuel salt. We will compare the data from these experiments with the data from the current experiment.

4. Conclusion

Candidate materials were subjected to exposure in a NaCl-$MgCl_2$ eutectic salt for 500 h within a natural convection loop, wherein the maximum nominal temperature reached 580°C. Throughout this experiment, the samples positioned in the hot leg of the natural convection loop decreased in mass, whereas the high-Ni alloy samples in the cold leg increased in mass. Notably, deposits were observed on the surfaces of the high-Ni alloy samples located on the cold leg. Furthermore, the sample exposed to the highest temperature of 580°C within the natural convection loop experienced a greater mass loss than that of the samples in the cold leg. The SS304 samples displayed the most adverse corrosion characteristics. Examination of the corroded samples revealed that Fe served as the principal constituent of the alloy deposited within the cold leg, accompanied by MgO deposits. Additionally, typical corrosion patterns characterized by the depletion of Cr near the surfaces were detected.

Data Availability

The data that support the findings of this study are available from the corresponding author upon reasonable request.

Conflicts of Interest

The authors declare that they have no conflicts of interest.

Acknowledgments

This work was supported by the Molten Salt Reactor Development Agency grant funded by the Korea government (Ministry of Science and ICT) (Project Number: RS-2023-00261146).

References

[1] R. C. Briant and A. M. Weinberg, "Molten fluorides as power reactor Fuels," *Nuclear Science and Engineering*, vol. 2, no. 6, pp. 797–803, 1957.

[2] B. C. Kelleher, S. F. Gagnon, and I. G. Mitchell, "Thermal gradient mass transport corrosion in NaCl-$MgCl_2$ and $MgCl_2$-NaCl-KCl molten salts," *Materials Today Communications*, vol. 33, article 104358, 2022.

[3] K. Goyal, H. Singh, and R. Bhatia, "Cyclic high temperature corrosion studies of carbon nanotubes-Cr_2O_3 composite coatings on boiler steel at 900°C in molten salt environment," *Anti-Corrosion Methods and Materials*, vol. 65, no. 6, pp. 646–657, 2018.

[4] M. Hong, H. L. Chan, J. R. Scully, and P. Hosemann, "Corrosion property of alloy 625 in molten FLiNaK salt according to the tellurium concentrations," *Journal of Nuclear Materials*, vol. 584, article 154548, 2023.

[5] Y. Wu, B. Leng, and X. Zhou, "Corrosion behaviors of Ni-WC cemented carbide in high temperature molten fluoride salt and vapor," *Journal of Nuclear Materials*, vol. 561, article 153541, 2022.

[6] M. Hu, X. Yang, X. Wang, H. Liu, X. Su, and X. Zhou, "Effect of Te on the corrosion behavior of GH3535 alloy in molten LiF-NaF-KF salt," *Corrosion Science*, vol. 227, article 111761, 2024.

[7] Y. Qin, C. Liu, C. Zheng et al., "The corrosion behavior of CVD SiC coatings on SiC_f/SiC composites in a simulated molten salt reactors environment," *Corrosion Science*, vol. 204, article 110411, 2022.

[8] K. Goyal, H. Singh, and R. Bhatia, "Hot corrosion behaviour of carbon nanotubes reinforced chromium oxide composite coatings at elevated temperature," *Materials Research Express*, vol. 5, article 116408, 2018.

[9] K. Hanson, K. Mo, P. F. W. Sankar et al., "Effect of excess Mg to control corrosion in molten $MgCl_2$ and KCl eutectic salt mixture," *Corrosion Science*, vol. 194, article 109914, 2022.

[10] J. Serp, M. Allibert, O. Benes et al., "The molten salt reactor (MSR) in generation IV: overview and perspectives," *Progress in Nuclear Energy*, vol. 77, pp. 308–319, 2014.

[11] T. J. Dolan, *Molten Salt Reactors and Thorium Energy*, Woodhead Publishing is an imprint of Elsevier, 2017.

[12] K. Sridharan and T. R. R. Allen, *Corrosion in Molten Salts*, Elsevier Inc, 2013.

[13] V. Ignatiev and A. Surenkov, "5 e Corrosion phenomena induced by molten salts in generation IV nuclear reactors," in *Structural materials for generation iv nuclear reactors*, pp. 153–189, Woodhead Publishing, 2017.

[14] E. S. Bettis, W. B. Cottrell, E. R. Mann, J. L. Meem, and G. D. Whitman, "The aircraft reactor experiment-operation 1,"

Nuclear Science and Engineering, vol. 2, no. 6, pp. 841–853, 1957.

[15] W. D. Manly, G. M. Adamson, J. H. Coobs et al., *Aircraft Reactor Experiment–Metallurgical Aspects. No. ORNL-2349*, Oak Ridge National Lab.(ORNL), Oak Ridge, TN (United States), 1957.

[16] S. S. Raiman, "Aggregation and data analysis of corrosion studies in molten chloride and fluoride salts," *Journal of Nuclear Materials*, vol. 511, pp. 523–535, 2018.

[17] S. S. Raiman, J. M. Kurley, D. Sulejmanovic et al., "Corrosion of 316H stainless steel in flowing FLiNaK salt," *Journal of Nuclear Materials*, vol. 561, article 153551, 2022.

[18] L. S. Richardson, D. C. Vreeland, and W. D. Manly, *Corrosion by molten fluorides, ORNL-1491*, Carbide and Carbon Chemical Company, 1952.

[19] J. W. Koger, *Effect of FeF_2 addition on mass transfer in a Hastelloy-N-LiFBeF_2-UF_4 thermal convection loop system, ORNL-TM-4188*, Oak Ridge National Lab, TennUSA, 1972.

[20] H. Susskind, F. B. Hill, S. Green et al., *Corrosion studies for a fused salt-liquid metal extraction process for the liquid metal fuel reactor, BNL-585*, Brookhaven National Lab.(BNL), Upton, NY (United States), 1960.

[21] C. J. Raseman, H. Susskind, G. Farber, and F. J. McNulty, *Engineering experience at Brookhaven National Laboratory in handling fused chloride salts, BNL-627*, Brookhaven National Lab.(BNL), Upton, NY (United States), 1960.

[22] L. C. Olson, R. E. Fuentes, M. J. Marinez-Rodriguez et al., "Impact of corrosion test container material in molten fluorides," *Journal of Solar Energy Engineering*, vol. 137, no. 6, article 061007, 2015.

[23] S. Guo, J. Zhang, W. Wu, and W. Zhou, "Corrosion in the molten fluoride and chloride salts and materials development for nuclear applications," *Progress in Materials Science*, vol. 97, pp. 448–487, 2018.

[24] R. B. Evans III, J. W. Koger, and J. H. DeVan, *Corrosion in polythermal loop systems II. A solid-state diffusion mechanism with and without liquid film effects, ORNL-4575*, Oak Ridge National Lab.(ORNL), Oak Ridge, TN (United States), 1971.

[25] M. Turkyilmazoglu, "Advective flow in a magnetized layer of fluid between hydro-thermal slippery parallel walls," *Archive of Applied Mechanics*, vol. 93, no. 12, pp. 4351–4360, 2023.

[26] D. Olander, "Redox condition in molten fluoride salts: definition and control," *Journal of Nuclear Materials*, vol. 300, no. 2-3, pp. 270–272, 2002.

[27] W. Doniger, C. Falconer, A. Couet, and K. Sridharan, "Corrosion of 316L & 316H stainless steel in molten LiF-NaF-KF (FLiNaK)," *Journal of Nuclear Materials*, vol. 579, article 154383, 2023.

[28] K. Duemmler, M. Woods, T. Karlsson, R. Gakhar, and B. Beeler, "First-principles-derived transport properties of molten chloride salts," *Journal of Nuclear Materials*, vol. 585, article 154601, 2023.

[29] W. Ding, H. Shi, A. Jianu et al., "Molten chloride salts for next generation concentrated solar power plants: mitigation strategies against corrosion of structural materials," *Solar Energy Materials and Solar Cells*, vol. 193, pp. 298–313, 2019.

[30] M. Kutz, *Handbook of Environmental Degradation of Materials*, William Andrew, 3rd edition, 2018.

[31] D. Fantozzi, V. Matikainen, M. Uusitalo, H. Koivuluoto, and P. Vuoristo, "Chlorine-induced high temperature corrosion of Inconel 625 sprayed coatings deposited with different thermal spray techniques," *Surface and Coatings Technology*, vol. 318, pp. 233–243, 2017.

[32] J. Zhang, C. W. Forsberg, M. F. Simpson et al., "Redox potential control in molten salt systems for corrosion mitigation," *Corrosion Science*, vol. 144, pp. 44–53, 2018.

[33] X. Yang, H. Liu, B. Chen, M. Ge, Y. Qian, and J. Wang, "Corrosion behavior of GH3535 alloy in molten LiF–BeF_2 salt," *Corrosion Science*, vol. 199, article 110168, 2022.

[34] B. A. Pint, J. M. Kurley, and D. Sulejmanovic, "Performance of alloy 600 in flowing commercial Cl salt at 600°-750°C," *AIP Conference Proceedings*, vol. 2445, no. 1, article 020011, 2022.